Sustainable Science and Innovation
https://ssi.ukscip.com

Article

A Mangrove-Inspired Off-Grid System Integrating Electrodialysis and Photothermal Evaporation for Direct Lithium Salt Extraction from Brine

Hongtian Liu [#], Kun Zhang [#], Changan Lu [#], Jia Liu, Kian Ping Loh [*]

Department of Chemistry, National University of Singapore, Singapore 117543, Singapore; e0708179@u.nus.edu (H.L.); cang7up@163.com (K.Z.); CHANGAN001@e.ntu.edu.sg (C.L.); liujia92@nus.edu.sg (J.L.)

[*] Correspondence: chmlohkp@nus.edu.sg

[#] These authors contributed equally: Hongtian Liu, Kun Zhang, Changan Lu.

Received: 25 July 2026; **Revised:** 18 August 2026; **Accepted:** 20 August 2026; **Published:** 31 August 2026

Citation: Liu, H.T.; Zhang, K.; Lu, C.; Liu, J.; Loh, K.P. A Mangrove-Inspired Off-Grid System Integrating Electrodialysis and Photothermal Evaporation for Direct Lithium Salt Extraction from Brine. *Sustain. Sci. Innov.* **2026**, *1*, 103130. https://doi.org/10.54963/ssi.103130

Abstract: The growing demand for lithium necessitates sustainable extraction technologies that overcome the high energy consumption and geographical constraints of traditional evaporation and chemical precipitation. Here, we report the first mangrove-inspired photothermal–electrodialysis (PT–ED) system that achieves self-sustained, selective, and direct lithium salt extraction using only solar energy. The system integrates photo–electro–thermal (PET) coupling, where sunlight-driven photothermal evaporation and internally generated electric fields synergistically regulate ion migration and water removal within a single continuous process. This coordinated field interaction enables directional Li^+ transport and controlled crystallization while preventing membrane fouling and parasitic salt deposition. Structural optimization of the leaf-shaped PT interface and an $Li_{0.33}La_{0.56}TiO_3$ (LLTO)-based Li^+-selective membrane ensures sustained operation and high selectivity. The PT–ED system delivers a Li^+ flux of 9.6 mg m^{-2} h^{-1} and Li^+/Mg^{2+} selectivity above 800, maintaining stable performance over 72 h and across brines collected from different salt lakes. This bioinspired PET approach offers a scalable pathway toward solar-driven, off-grid lithium recovery, establishing a universal framework for sustainable ion extraction, solar desalination, and circular water–energy utilization.

Keywords: Li extraction; mangrove; photothermal–electrodialysis system

1. Introduction

The accelerating electrification of transportation and large-scale energy storage has made lithium indispensable to the global clean-energy transition.[1–3] Yet, conventional lithium extraction from hard-rock ores and continental brines remains energy-intensive, geographically constrained, and environmentally disruptive.[4,5] Multi-stage evaporation and chemical precipitation require vast land areas, extensive freshwater use, and long residence times, leading to high carbon and water footprints.[6,7] As lithium demand continues to surge, developing a sustainable, low-carbon, and geographically adaptable extraction pathway has become an urgent global priority. Among emerging routes, solar-driven extraction is particularly attractive for its ability to directly harness renewable energy while minimizing chemical input and process complexity.[8–11]

Current lithium extraction processes typically follow a multi-step sequence: ion separation, filtration, evaporation, and precipitation, each consuming substantial energy and generating cumulative losses.[12,13] Due to the technology advancement and the large-scale application of lithium-ion batteries in recent years, the market demand for lithium is growing rapidly and the availability of land lithium resources is decreasing significantly. As such, the focus of lithium extraction technologies has shifted to water lithium resources involving salt-lake brines and sea water.[3] Among various aqueous recovery technologies, the lithium ion-sieve (LIS) technology is considered the most promising one. This is because LISs are excellent adsorbents with high lithium uptake capacity, superior lithium selectivity and good cycle performance. These attributes have enabled LISs to separate lithium effectively from aqueous solutions containing different ions.[14,15] Besides, some common LIS composite materials forming technologies, including granulation, foaming, membrane and fiber formation, and magnetization,

Copyright © 2026 by the author(s). Published by UK Scientific Publishing Limited. This is an open access article under the Creative Commons Attribution (CC BY) license (https://creativecommons.org/licenses/by/4.0/).

which are used to overcome the shortcomings in industrial column operations, are also explored.[16–19] This segmented workflow prolongs production cycles and limits scalability (Figure 1a). Recent advances in solar-driven systems, such as photothermal or transpiration-based evaporators, have introduced greener alternatives but still operate as independent enrichment units that require downstream crystallization and purification.[8,10] In contrast, a one-step "brine-to-salt" process that integrates ion selection, concentration, and crystallization within a single device would represent a transformative leap in lithium recovery. Such a continuous, direct-salt approach could dramatically shorten extraction times, eliminate intermediate reagents, and enable decentralized, off-grid operation, achieving the same conceptual revolution that solar desalination brought to traditional distillation (Figure 1b).

However, realizing this one-step lithium extraction requires overcoming the intrinsic limitations of purely photothermal systems, whose ion transport is governed by diffusion and capillary effects. These passive systems lack directional driving forces and controllable interfaces, leading to sluggish ion kinetics and poor selectivity among coexisting cations such as Na^+, K^+, and Mg^{2+}. Moreover, while photothermal heating can locally concentrate brine, it cannot continuously direct Li^+ migration or achieve controlled crystallization. Nature provides an instructive blueprint for such coordinated field coupling. Mangroves, thriving in hypersaline coastal environments, maintain ionic homeostasis by integrating osmotic, electrical, and thermal gradients through their root–stem–leaf hierarchy.[20,21] Their roots selectively absorb water and reject salt; trunks mediate ion transport; and leaves drive evaporation via solar heating. Inspired by this biological architecture, we designed a mangrove-inspired PET lithium extraction system that unifies root-like ion selection, trunk-like solution transport, and leaf-like photothermal evaporation into a single, self-sustaining platform (Figure 1b). At the "roots", ED selectively captures Li^+ while excluding competing ions. The "trunk" functions as a circulating catholyte channel that stabilizes flow and prevents membrane fouling, while the "leaves" concentrate solar energy to drive direct crystallization of lithium salts. This integrated "artificial mangrove" converts the traditional four-step extraction sequence into a one-step solar-powered process, eliminating external power and post-treatment requirements. Here, "self-sustained" signifies that the system operates entirely off-grid: solar heat directly drives the photothermal evaporation, while a coupled solar panel (simulated by a 3 V DC power supply in laboratory tests) provides the requisite electric field for the electrodialysis module.

Herein, we report that this bioinspired PET system achieves self-sustained, high-selectivity lithium recovery and direct lithium salt formation using only solar energy as the primary input. As is shown in Figure 1b, the synergistic operation of photothermal heating and photo-induced electric potential establishes a dynamic, directional ion-transport regime, as confirmed by operando measurements and multiphysics simulations. This coupled-field regulation enhances Li^+/Mg^{2+} discrimination by over an order of magnitude compared with photothermal-only systems, while enabling stable, autonomous operation under natural sunlight. Benefiting from its integrated mechanism and modular architecture, the PET device delivers > 800 Li^+ selectivity and completes the entire brine-to-salt conversion in a single, continuous step.

2. Result and discussion

The constructed flow cell is shown in Figure 1c, and its internal structure is illustrated in Figure 1d. The cell is composed of three functional layers: a brine channel, a lithium extraction channel, and a Li^+-selective membrane sandwiched between them to enable directional ion transport. The top layer serves as a photothermal evaporation interface, where concentrated lithium solution undergoes sunlight-driven crystallization. To enable efficient and continuous lithium extraction from dilute brines, our system design integrates two core modules: ED for selective ion separation and PT evaporation for salt crystallization. This dual-module configuration ensures both high ion selectivity and autonomous brine concentration under solar irradiation. However, achieving coordinated operation between these two modules requires a coherent theoretical foundation to synchronize ion transport and water removal governed by vastly different mechanisms. In the ED module, Li^+ flux is driven by an internally generated electric field and described by the extended Nernst–Planck equation,[22–24] allowing precise modulation of migration rate and selectivity. In parallel, the PT module sustains continuous evaporation through capillary-fed water supply and Knudsen-dominated vapor transport,[10,25] efficiently converting solar energy into localized thermal gradients. By coupling these electrochemical and thermodynamic transport principles, a flux-matching strategy is established to balance Li^+ migration and solvent evaporation, thereby maintaining operational stability and maximizing extraction efficiency. The following sections elaborate the theoretical basis of each subsystem and the interfacial coordination that underpins their integrated performance.

Building on the above conceptual framework, the theoretical foundation of the coupled PT–ED system can be established by quantitatively describing the transport processes in both subsystems. In the ED section, lithium-ion migration under an externally applied electric field follows the extended Nernst–Planck equation:[23,24]

$$J_e = -D_{Li}\frac{dC_{Li}}{dx} - \left(D_{Li}\frac{z_{Li}F}{RT}C_{Li}\frac{d\psi}{dx}\right) + vC_{Li} \qquad (1)$$

where J_e is the flux of the Li^+, consisting of the diffusive, electromigrative and convective terms respectively, in the order they appear in the equation. Where, D_{Li} is the diffusion coefficient for Li^+ in the membrane, C_{Li} is the local Li^+ concentration, z_{Li}

Sustain. Sci. Innov. **2026**, *1*, 103130
https://doi.org/10.54963/ssi.v1i1.103130

is the ionic charge (+1 for Li^+), F and R are the Faraday and gas constants, respectively, T is the absolute temperature, ψ is the membrane potential, and v is the average velocity of convective solvent flow. Among these terms, the electric field commonly dominates, driving the migration of Li^+ more efficiently than diffusion or convective flow. Such dominance is advantageous for selective extraction: by fine-tuning the applied voltage, one can favor Li^+ transport over other ions in the feed. This precise control of Li^+ migration forms the basis for integrating ED with downstream processes, ensuring that the brine exiting the ED section arrives at suitable concentration and flow conditions for subsequent operations.

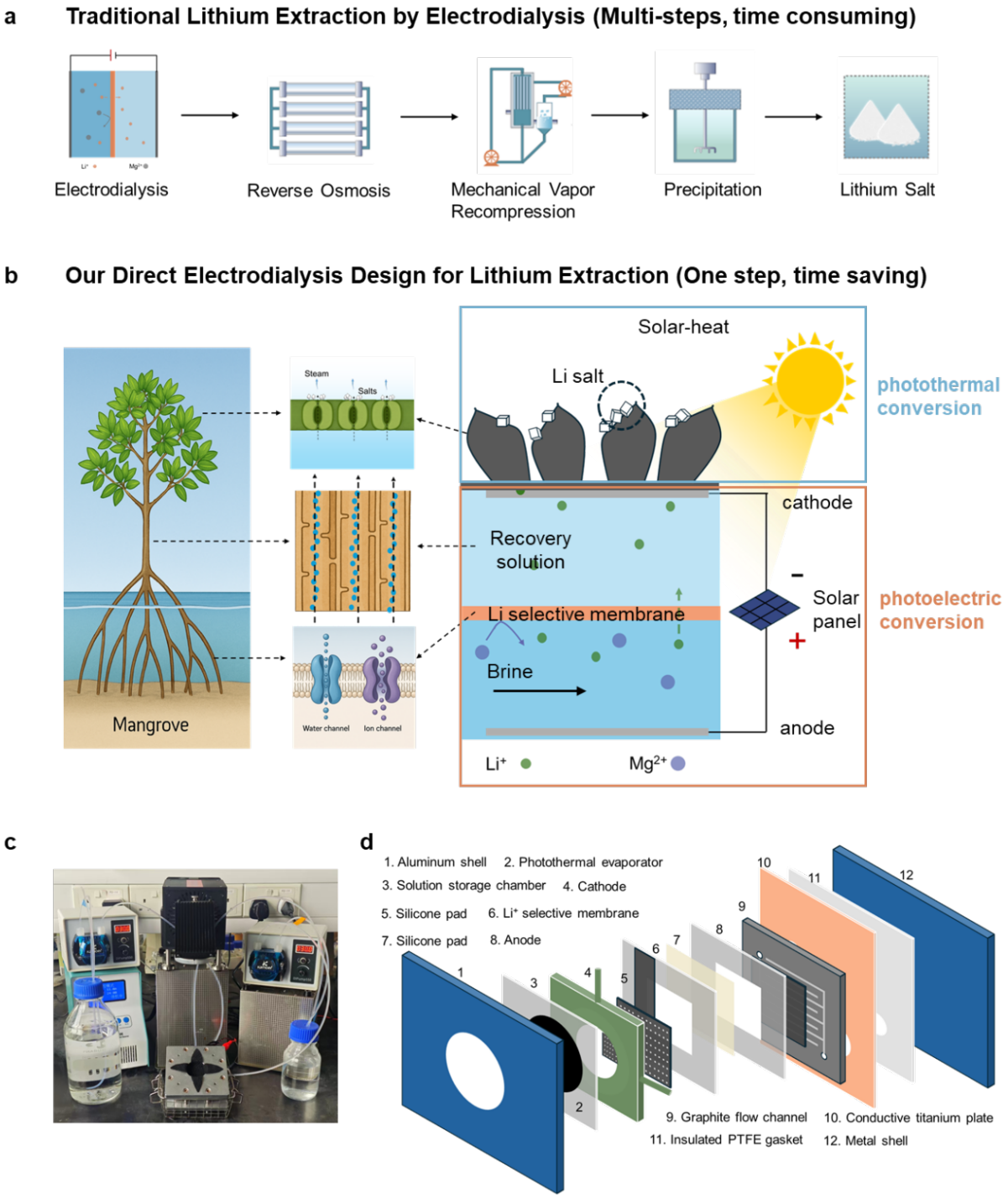


Figure 1. Comparison of different lithium extraction methods and structural design of the integrated PT–ED system. (**a**) General process of conventional lithium extraction. (**b**) Schematic illustration of the mangrove-inspired system integrating electrodialysis and photothermal evaporation for direct lithium extraction. (**c**) Digital photographs of the as-prepared PT–ED device. (**d**) Schematic illustration showing the detailed construction and composition of the flow cell.

Sustain. Sci. Innov. **2026**, *1*, 103130
https://doi.org/10.54963/ssi.v1i1.103130

In the PT evaporation section, water molecules continuously evaporate through the porous transport layer driven by capillary forces and solar-induced heating. The capillary pressure that sustains liquid supply follows the Young–Laplace equation:[26,27]

$$P = \frac{2\gamma\, cos\theta}{r} \tag{2}$$

where γ is the water surface tension, θ is the water contact angle on the pore surface, and r is the pore radius. Smaller pore sizes and more hydrophilic surfaces (lower θ) generate higher capillary pressures, ensuring a steady replenishment of water for evaporation, as is illustrated in Figure 2b. To achieve a high transpiration flux (J_p), we leveraged Knudsen-dominated vapor transport within small pores. Under these conditions, molecule-wall collisions dominate, and the flux J:[10,25]

$$J_p = \frac{2}{3}\frac{\varepsilon}{\tau}\frac{r}{\delta}\sqrt{\frac{8RT}{\pi M}}\left[p_{sat}(T) - p_{v,environment}\right] \tag{3}$$

where J (kg m^{-2} h^{-1}) is the vaporization or permeation flux of water, ε is the membrane porosity, τ is the pore tortuosity, r is the average pore radius, δ is the membrane thickness, R is the gas constant, M is the molar mass of water, T is the absolute temperature, $p_{sat}(T)$ is the saturation vapor pressure of water at temperature T, and $p_{v,environment}$ is the partial pressure of water vapor on the membrane's opposite side or in the surrounding environment (often relatively low under atmospheric conditions).

In situations where membrane porosity, tortuosity, and thickness can be partially neglected, this expression simplifies to:

$$J_{sim} = \alpha r T\left[p_{sat}(T) - p_{v,environment}\right] \tag{4}$$

where α is a coefficient encapsulating geometric factors, fundamental constants, and unit conversions. The simplified relationship underscores that increasing the pore radius or the operational temperature both enhance the flux (Figure 2c). However, a larger pore radius diminishes the transpiration pressure, creating a design trade-off between driving force and vapor flux.

Bringing these two sections together, our integrated ED-PT platform seeks a balance between the ion flux from the ED compartment (J_e) and the evaporative flux in the photothermal section (J_p). Under steady-state operation, matching these fluxes:

$$J_e = J_p \tag{5}$$

prevents both undesired precipitation within the ED module (which would occur if $J_e \gg J_p$) and membrane drying in the PT compartment (if $J_p \gg J_e$). Thus, the principle for optimization centers on integrating ED selectivity with photothermal evaporation efficiency. By coordinating these fluxes, lithium-rich brine is delivered to the PT membrane at the precise rate needed for continuous and controlled salt precipitation.

Based on the above theoretical analysis, the photothermal evaporator was rationally designed to satisfy the flux-matching and capillary–evaporation criteria predicted by the model. The device consists of two key components: a water–salt transport membrane layer and a surface-adhered black photothermal fabric (Figure 2a). The transport layer continuously delivers lithium salt solution from the storage chamber to the evaporation interface, where the photothermal layer absorbs solar energy and accelerates water evaporation, leaving lithium salts behind. A commercially available hydrophilic polyether sulfone (PES) membrane (Figure 2d) was selected as the transport layer owing to its moderate wettability, with a contact angle of approximately 65°, enabling efficient capillary-fed water replenishment.[28,29] SEM imaging reveals a uniform porous morphology with an average pore radius of ~50 nm and an effective thickness of ~50 μm (Figure S1), both of which facilitate rapid saline flow across the membrane. According to Equation (2), these structural parameters correspond to a transpiration pressure of approximately 12 bar at 30 °C ($\gamma \approx 0.071$ N m^{-1}), as illustrated in Figure S2, providing sufficient driving force for continuous water transport under solar heating. The black photothermal top layer increases the rate of evaporation. Efficient absorption of broad-spectrum sunlight and rapid conversion to localized heat are crucial to sustain the vapor flux described by Equations (3) and (4), while simultaneously maintaining fast water diffusion to the surface. To meet these functional requirements, a bamboo-charcoal fiber cloth was chosen as the photothermal layer (Figure 2e). Its rough, interconnected fibrous texture enhances light trapping and promotes capillary-driven water spreading across the surface, thereby ensuring efficient coupling between thermal energy localization and liquid replenishment.

The optimized photothermal evaporator exhibits excellent broadband light absorption, reaching an average absorbance of 97% across the visible range (Figure 2f). This strong light-harvesting ability ensures efficient solar energy utilization for vapor generation. To evaluate its photothermal conversion performance, the surface temperature evolution was monitored under 3-sun illumination using an infrared thermal imager (Figure 2g). The surface temperature increased rapidly from 25 °C to 44 °C within 2 min and stabilized at 54 °C after 6 min, confirming fast heat localization and efficient photothermal conversion. Such high conversion efficiency originates from the combined effects of broadband light absorption and nonradiative plasmonic decay, which enable effective solar-to-thermal energy conversion at the liquid–vapor interface. Benefiting from this optimized design, the evaporator achieved a high transpiration rate of 2.1 L m^{-2} h^{-1} under one-sun illumination (Figure S3), outperforming most reported polymer-based evaporators. Moreover, it maintained stable long-term evaporation over continuous operation for 72 h (Figure 2h), demonstrating excellent thermal management and structural robustness

Sustain. Sci. Innov. **2026**, *1*, 103130
https://doi.org/10.54963/ssi.v1i1.103130

crucial for sustainable brine concentration and lithium-salt crystallization.

Initially, a circular photothermal layer with the same area as the PES membrane was employed. However, during continuous operation in 0.1 M LiCl solution, salt rapidly crystallized directly on the membrane surface (Figure 3a,d), progressively blocking the pores and hindering both water evaporation and lithium salt recovery. To mitigate this issue, a leaf-shaped photothermal structure was introduced to regulate the flow and crystallization pathways of the brine. The radial arms of this structure promote the upward migration of the salt solution along the arm channels, leading to preferential crystallization at the outermost tips rather than at the center (Figure 3b,e). This morphology-guided salt separation effectively prevents central pore clogging and enables sustained, stable evaporation over extended operation.

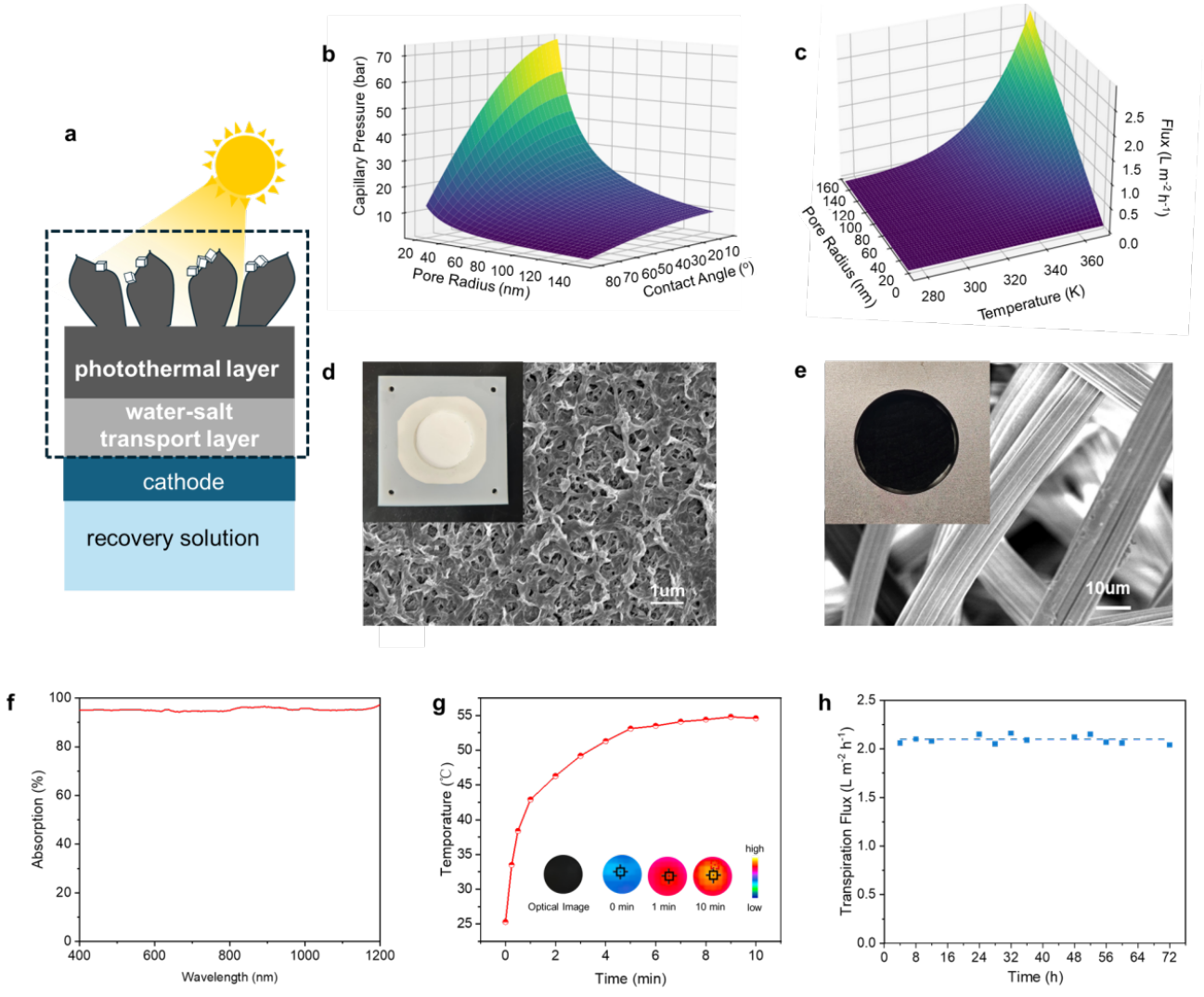


Figure 2. Structural design and experimental demonstration of the photothermal components. (**a**) Schematic illustration showing the detailed double-layer structure of photothermal components. (**b**) Transpiration pressure (P) as a function of contact angle and pore radius of the water–salt transport layer. (**c**) Transpiration flux as a function of temperature and pore radius of the photothermal layer. (**d**) Surface SEM image of the PES membrane, showing its porous morphology with an average pore radius of ~50 nm; inset: photograph of the commercial PES membrane module. (**e**) SEM image of the photothermal layer composed of black bamboo charcoal fiber cloth; inset: photograph of the photothermal layer. (**f**) Light absorption spectrum of the photothermal evaporator. (**g**) Time-dependent surface temperature of the photothermal evaporator under 1 sun illumination (1 kW m^{-2}). (**h**) Transpiration fluxes through the photothermal evaporators over a 72-h period at 1 kW m^{-2}.

Further optimization revealed that the arm length of the leaf-shaped structure critically governs the spatial distribution of salt crystallization. In the large-leaf design, the arms are approximately 5.5 cm long, whereas the small-leaf design features ~3 cm arms (Figure S4). Due to gravitational bending, the long-leaf configuration tends to curve slightly downward after assem-

Sustain. Sci. Innov. **2026**, *1*, 103130
https://doi.org/10.54963/ssi.v1i1.103130

bly (Figure 3i, inset), forming a concave surface where brine accumulates and evaporation becomes most intense at the curvature apex. As a result, premature salt crystallization occurs at intermediate positions before the solution can reach the outermost tips (Figure 3c,f). The time-dependent crystallization process of the leaf-shaped evaporator is illustrated in Figure S5. In contrast, the short-leaf configuration remains rigid and oriented upward, enabling continuous capillary-driven transport of the brine toward the extremities, where salt ultimately crystallizes at the apex (Figure 3h). Quantitative comparison of total crystallized mass indicates that the large-leaf structure achieves the highest salt recovery, yielding 0.52 g of precipitated salt after 36 h, markedly higher than that of the circular design (0.35 g, Figure 3g), while maintaining stable evaporation fluxes throughout operation. These findings confirm that the leaf-inspired photothermal geometry effectively regulates ion and water migration through controlled capillary pathways and localized thermal gradients, thereby enabling spatially selective salt crystallization and ensuring sustained, unimpeded operation of the PT–ED lithium extraction system. Consequently, the large-leaf configuration was selected as the optimal PT design for subsequent integrated experiments.

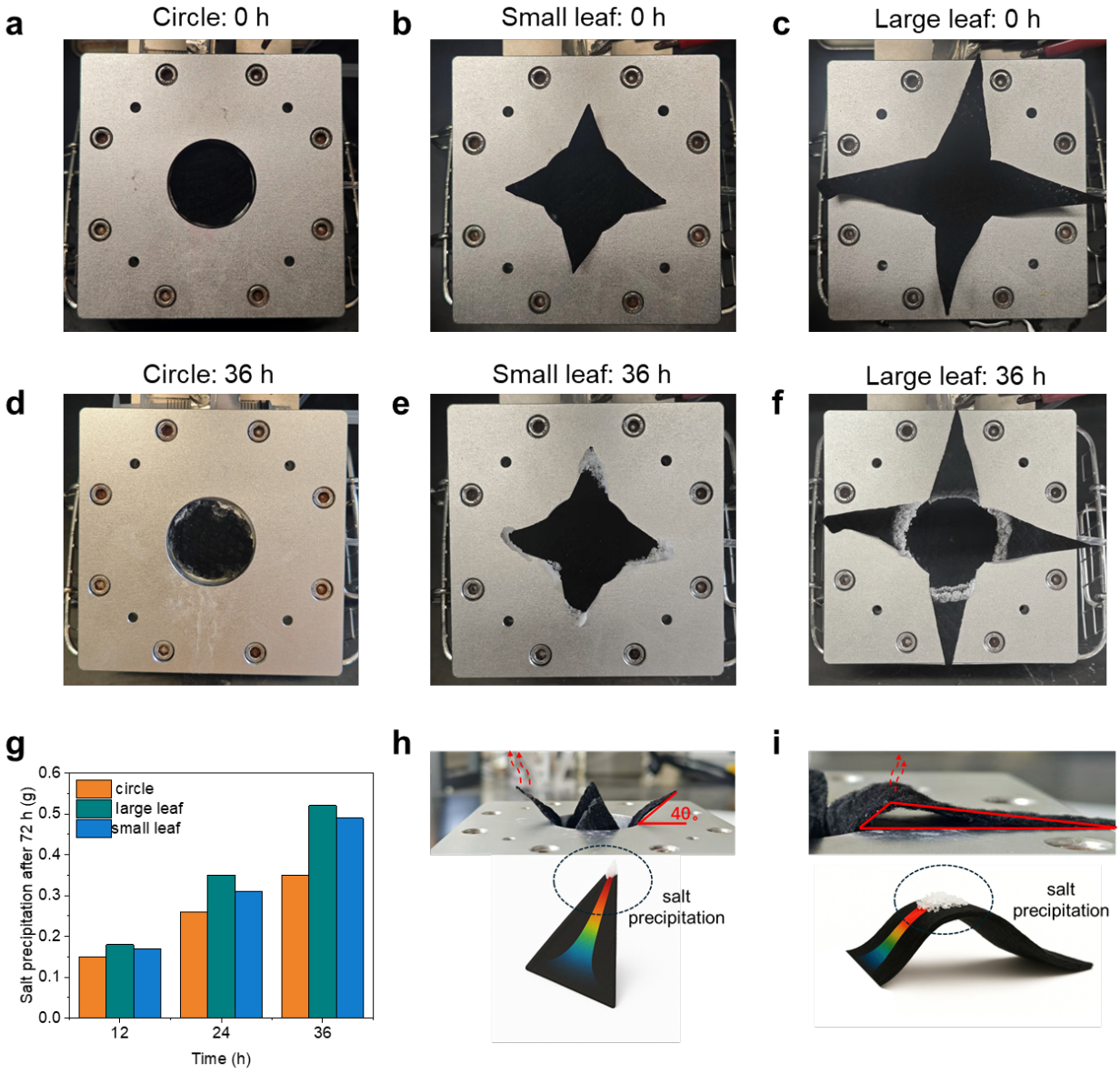


Figure 3. Shape design of the photothermal components. (**a–f**) Photographs showing salt crystallization in 0.1 M LiCl solution using photothermal components of different shapes under 1 kW m^{-2} simulated sunlight at 0 h and 36 h: (**a**,**d**) circular; (**b**,**e**) small leaf; (**c**,**f**) large leaf. (**g**) Comparison of the amounts of salt crystallization for different shapes. (**h**,**i**) Distinct salt crystallization sites observed for the small-leaf (**h**) and large-leaf (**i**) photothermal components.

Sustain. Sci. Innov. **2026**, *1*, 103130
https://doi.org/10.54963/ssi.v1i1.103130

The partially enriched solution collected from the photothermal evaporator is continuously circulated within a storage chamber that stabilizes the lithium-ion concentration and mitigates membrane fouling. A miniature pump with a constant flow rate of ~50 mL min^{-1} ensures homogeneous mixing and steady transport toward the evaporator, thereby preventing localized crystallization and flow blockages. Importantly, this circulating buffer, combined with the self-regulating capillary draw of the PES membrane, allows the system to tolerate transient mismatches between the electrodialysis flux and fluctuating photothermal evaporation rates, ensuring stable operation without requiring external flow control. The root-ED system serves as the primary driving module for transporting lithium ions from the brine to the recovery chamber. It consists of an anode feed compartment and a cathode recovery compartment, separated by a Li^+-selective membrane that allows directional ion migration. The anode is coated with a Ru–Ir catalyst, which efficiently catalyzes the oxidation of chloride ions to chlorine gas, maintaining charge balance during lithium extraction. The anodic reaction proceeds as:

$$R1: 2Cl^- - 2e^- \rightarrow Cl_2 \uparrow$$

To ensure environmental sustainability, the evolved chlorine gas is systematically collected and neutralized using an alkaline scrubber (e.g., NaOH solution), safely converting it into sodium hypochlorite.

At the cathode, a Pt/C catalyst, known for its excellent hydrogen evolution performance, facilitates the reduction of water to hydrogen gas:

$$R2: 2H_2O + 2e^- \rightarrow H_2 + 2OH^- \uparrow$$

The consumption of hydrogen ions lowers the proton concentration near the cathode, promoting the migration of Li^+ ions across the selective membrane to maintain charge neutrality. Under an applied electric field, the root-ED module operates continuously, driving Li^+ transport from the brine (anode side) to the recovery chamber (cathode side). Compared with conventional photothermal-only evaporation, this electrochemically assisted mechanism significantly enhances ion transport kinetics, as the electric field directly accelerates Li^+ migration rather than relying solely on slower, diffusion-driven processes.

The integrated architecture of the PT–ED system is illustrated in Figure 4a, which couples a root-ED module with a leaf-inspired PT interface. The ED unit functions as the "root," selectively extracting lithium ions from brine and driving them across the Li^+-selective membrane under an applied electric field. The permeated Li^+ solution is then transported to the "leaf" region, where photothermal evaporation induces localized crystallization along the outer edges, mimicking the salt exclusion and water transpiration processes of natural mangroves. This integrated configuration unifies ion migration, concentration, and crystallization into a single, continuous operation cycle.

To demonstrate the universality and scalability of the PT–ED platform, a commercial nanofiltration (NF) membrane was first employed as the Li^+-selective layer (Figure 4b,c). Although the NF membrane lacks intrinsic ion selectivity, it provides a useful benchmark for evaluating system compatibility. Under photothermal-only operation, the Li^+ flux was limited to 0.75 mg m^{-2} h^{-1} with a Li^+/Mg^{2+} selectivity of ~5. When coupled with electrodialysis, the Li^+ flux increased dramatically to 23 mg m^{-2} h^{-1}, while selectivity improved to ~8, confirming the synergistic contribution of the electric field in directing ion migration. During extended operation (Figure S6), the flux gradually declined from 23 to ~16 mg m^{-2} h^{-1} due to partial pore blockage, yet the selectivity rose to ~11, as the hindered water flow preferentially suppressed Mg^{2+} transport. These results demonstrate that even in the absence of specific Li^+ pathways, the PT–ED platform can leverage electro-driven transport and water-mediated coupling to achieve continuous lithium extraction, highlighting its technological versatility and application potential.

However, the limited ion selectivity of polymer-based NF membranes constrains their separation performance. To overcome this, a self-fabricated LLTO/ceramic membrane with intrinsic Li^+ conduction channels was incorporated (Figure 4d,e).[19] Unlike polymeric membranes, the LLTO membrane cannot operate under pure photothermal conditions, and an electric potential is essential to activate Li^+ migration through its solid-state lattice. Once integrated into the PT–ED platform, the LLTO membrane achieved a Li^+ flux of 9.6 mg m^{-2} h^{-1} and a Li^+/Mg^{2+} selectivity of 648, substantially outperforming conventional ED (8.3 mg m^{-2} h^{-1}, 614). This enhancement originates from photo–electro–thermal coupling, which synchronizes directional Li^+ transport with localized crystallization at the photothermal interface, maintaining a stable concentration gradient and minimizing back-diffusion. To explicitly distinguish the individual contributions within the PET coupling mechanism, it is important to note that the electric field (ED module) provides the dominant directional driving force for Li^+ migration. Concurrently, the photothermal (PT) module acts as a continuous water-removal and crystallization sink. By coupling these two processes, the PT module effectively prevents localized Li^+ accumulation and concentration polarization on the permeate side of the selective membrane. This synergistic coordination maintains a stable transmembrane concentration gradient and minimizes Li^+ back-diffusion, which fundamentally explains why the integrated PT–ED system achieves a higher overall extraction flux and selectivity than independent ED operation.

Sustain. Sci. Innov. **2026**, *1*, 103130
https://doi.org/10.54963/ssi.v1i1.103130

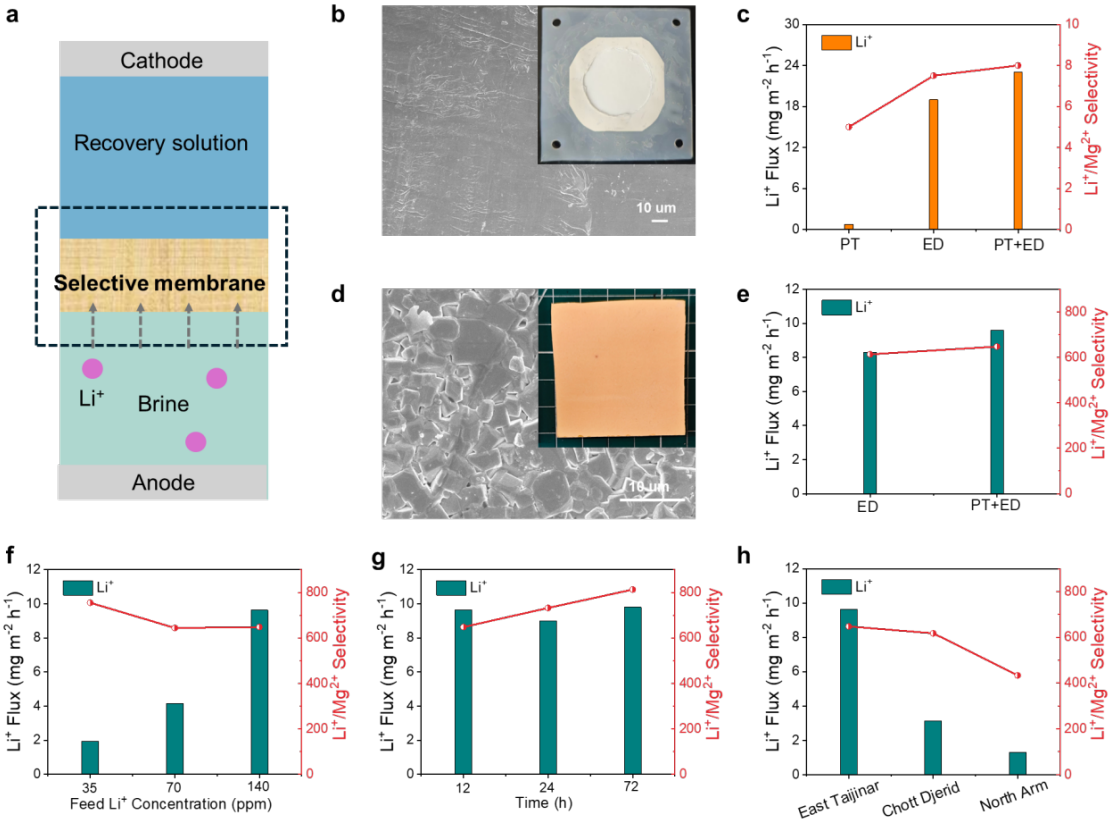


Figure 4. Structural design and electrochemical performance of Li^+-selective membranes in the PT–ED system. (**a**) Schematic illustration showing the detailed structure near the Li^+-selective membrane. (**b**) SEM image of the commercial nanofiltration membrane used as the Li^+-selective layer; inset: digital photograph of the membrane. (**c**) Comparison of Li^+ flux and Li^+/Mg^{2+} selectivity under photothermal-only, electrodialysis-only, and combined PT–ED modes using the nanofiltration membrane. (**d**) SEM image of the self-fabricated LLTO/ceramic membrane used as the Li^+-selective layer; inset: digital photograph of the membrane. (**e**) Comparison of Li^+ flux and Li^+/Mg^{2+} selectivity under electrodialysis-only and PT–ED modes using the LLTO/ceramic membrane. (**f**) Effect of total ion concentration on PT–ED performance at a fixed Li^+/Mg^{2+} ratio of 60:1 using the LLTO/ceramic membrane. (**g**) Long-term stability test of PT–ED over 72 h with the LLTO/ceramic membrane. (**h**) Evaluation of the PT–ED platform for lithium extraction from different brines using the LLTO/ceramic membrane.

To further assess the operational robustness of the LLTO-based PT–ED system, a series of comparative and long-term tests were conducted (Figure 4f–h). When the Li^+/Mg^{2+} ratio was fixed at 60:1, increasing the total ionic strength from 35 ppm to 140 ppm resulted in a nearly fivefold enhancement of Li^+ flux (from 1.9 to 9.6 mg m^{-2} h^{-1}), while the Li^+/Mg^{2+} selectivity remained constant (~650–750). This concentration-insensitive behavior underscores the stability of the LLTO's Li^+ conduction channels, which are less affected by electrostatic screening or ion competition than polymeric systems. During continuous operation for 72 h (Figure 4g), the Li^+ flux remained steady (~9–10 mg m^{-2} h^{-1}), while the selectivity increased from 648 to 812, reflecting cumulative Li^+ enrichment and progressively reduced Mg^{2+} permeability. The corresponding lithium accumulation reached ~706 mg m^{-2} after 72 h (Figure S7), confirming the stable coupling between Li^+ transport and localized crystallization at the PT interface. Driven by the remarkably high Li^+/Mg^{2+} selectivity of the LLTO membrane confirmed via ICP-OES, the ionic composition of the solution delivered to the photothermal interface is overwhelmingly dominated by lithium. This ensures that the final localized crystallization yields highly pure solid lithium salts, validating the direct 'brine-to-salt' capability of the system. Furthermore, despite the continuous generation of OH^- at the cathode, the macroscopic performance remained highly stable. The rapid circulation of the recovery solution prevents severe localized pH accumulation, ensuring that the chemical and structural integrity of the LLTO membrane and photothermal components are maintained, as evidenced by the steady Li^+ flux and sustained selectivity over 72 h. Finally, the adaptability of the PT–ED platform was examined using brines from three representative salt lakes: East Taijinar (China), Chott Djerid (Tunisia), and North Arm (USA) (Table S1, Figure 4h). The system exhibited the highest performance in East Taijinar brine (Li^+ flux = 9.6 mg m^{-2} h^{-1}, selectivity = 648). As the Li^+ concentration decreased and Li^+/Mg^{2+} ratio increased in other sources, the flux and selectivity declined to 3.1 mg m^{-2} h^{-1}/618 for Chott Djerid

Sustain. Sci. Innov. **2026**, *1*, 103130
https://doi.org/10.54963/ssi.v1i1.103130

and 1.3 mg m^{-2} h^{-1}/434 for North Arm. These results confirm that the PT–ED platform performs optimally in moderately concentrated brines but remains operable even under harsh separation conditions, demonstrating strong environmental adaptability and scalability for real-world lithium recovery. Compared with previously reported lithium extraction technologies, the mangrove-inspired PT–ED system demonstrates distinct advantages across key operational parameters. Conventional electrodialysis systems typically require continuous and substantial grid electricity and often struggle with moderate selectivity when processing complex brines. Conversely, standalone photothermal evaporators operate with low energy consumption but suffer from sluggish, diffusion-driven ion kinetics, resulting in inferior Li^+ fluxes and low selectivity. Our integrated PET approach effectively bridges this gap. By directly coupling solar-driven evaporation with an internal electric field, the system achieves a competitive Li^+ flux of 9.6 mg m^{-2} h^{-1} and a superior Li^+/Mg^{2+} selectivity exceeding 800. Furthermore, the system exhibits excellent operational stability over 72 h without membrane fouling or performance degradation. Crucially, by relying solely on solar energy as the primary input, this off-grid architecture bypasses the high energy consumption of traditional industrial processes, offering a highly sustainable and competitive framework for direct lithium salt recovery.

3. Conclusion

We have developed a mangrove-inspired PT–ED system that achieves self-sustained, selective, and direct lithium salt extraction from brines using only solar energy as the primary input. By integrating field-driven ED with sunlight-powered PT evaporation, the PT–ED architecture unifies ion separation, solution transport, and crystallization within a single continuous process, transforming conventional multi-stage lithium recovery into a one-step, off-grid operation. Through theoretical analysis and flux-matching design, the coupled PET mechanism was elucidated, revealing how coordinated ion migration and water evaporation synergistically enhance lithium flux while preventing parasitic crystallization or membrane drying. Structural optimization of the leaf-shaped PT interface ensured sustained capillary water delivery and spatially controlled salt precipitation, while the LLTO-based Li^+-selective membrane enabled high ionic selectivity and long-term stability. The integrated PT–ED system demonstrated Li^+ fluxes up to 9.6 mg m^{-2} h^{-1} and Li^+/Mg^{2+} selectivity exceeding 800, maintaining stable operation over 72 h and achieving direct lithium salt crystallization without external reagents or power. Its consistent performance across diverse brines highlights the system's broad environmental adaptability and scalability for real-world deployment. This work establishes a generalized bioinspired strategy for coupling multiple driving fields to achieve sustainable ion extraction. Beyond lithium, the PT–ED framework provides a blueprint for renewable, off-grid recovery of critical elements from complex aqueous environments, offering a pathway toward solar desalination, and circular water–energy systems.

Supporting Information

The Supporting Information is available free of charge at https://ssi.ukscip.com/uploads/7/asset-file/2026/09/asset-file_75dbac28321c19984ce220530ff94cb0.pdf.

Author Contributions

Conceptualization, H.L., K.Z. and C.L.; methodology, H.L., K.Z. and C.L.; validation, H.L., K.Z. and C.L.; formal analysis, H.L., K.Z., C.L., J.L.; investigation, H.L.; resources, H.L., K.Z. and C.L.; data curation, H.L., K.Z. and C.L.; writing—original draft preparation, H.L.; writing—review and editing, K.Z. and K.P.L.; supervision, K.P.L.; project administration, K.P.L.; funding acquisition, K.P.L. All authors have read and agreed to the published version of the manuscript.

Data Availability Statement

Data are available from the corresponding authors upon reasonable request.

Funding

This research was supported by the National Research Foundation (NRF), Singapore and implemented by the Public Utilities Board (PUB), Singapore's National Water Agency, under its Competitive Funding for Water Research Funding Initiative (grant award CWR-2101-0032). Any opinions, findings and conclusions or recommendations expressed in this material are those of the author(s) and do not reflect the views of NRF and PUB.

AI Use Statement

The authors declare that no artificial intelligence (AI) tools were used in the preparation of this manuscript.

Conflict of Interest

The authors declare no conflict of interest.

References

1. Lu, D.; Li, R.; Rahman, M.M.; Yu, P.; Lv, L.; Yang, S.; Huang, Y.; Sun, C.; Zhang, S.; Zhang, H.; et al. Ligand-Channel-Enabled Ultrafast Li-Ion Conduction. *Nature* **2024**, *627*, 101–107. [CrossRef]
2. Zhang, K.; Liu, W.; Gao, Y.; Wang, X.; Chen, Z.; Ning, R.; Yu, W.; Li, R.; Li, L.; Li, X.; et al. A High-Performance Lithium Metal Battery with Ion-Selective Nanofluidic Transport in a Conjugated Microporous Polymer Protective Layer. *Adv. Mater.* **2021**, *33*, 2006323. [CrossRef]
3. Yang, S.; Wang, Y.; Pan, H.; He, P.; Zhou, H. Lithium Extraction from Low-Quality Brines. *Nature* **2024**, *636*, 309–321.

Sustain. Sci. Innov. **2026**, *1*, 103130
https://doi.org/10.54963/ssi.v1i1.103130

[CrossRef]
4. Li, Z.; Chen, I.-C.; Cao, L.; Liu, X.; Huang, K.-W.; Lai, Z. Lithium Extraction from Brine through a Decoupled and Membrane-Free Electrochemical Cell Design. *Science* **2024**, *385*, 1438–1444. [CrossRef]
5. Zheng, H.; Fan, J.; Chen, A.; Li, X.; Xie, X.; Liu, Y.; Ding, Z. Enhancing Solar-Driven Water Purification by Multiscale Biomimetic Evaporators Featuring Lamellar MoS_2/GO Heterojunctions. *ACS Nano* **2024**, *18*, 3115–3124. [CrossRef]
6. Zhang, G.; Li, Y.; Guan, X.; Hu, G.; Su, H.; Xu, X.; Feng, G.; Shuchi, S.B.; Kim, S.C.; Zhou, J.; et al. Spontaneous Lithium Extraction and Enrichment from Brine with Net Energy Output Driven by Counter-Ion Gradients. *Nat. Water* **2024**, *2*, 1091–1101. [CrossRef]
7. Wu, Y.; Zhai, M.; Tian, S.; Yuan, H.; Luo, X.; Huang, G.; Fu, Y.; Zhu, M.; Gu, Y.; Huan, W.; et al. A Circular Economy Approach for the Global Lithium-Ion Battery Supply Chain. 2025, *In Review*. [CrossRef]
8. Wang, Y.; Zhao, W.; Peng, Z.; Feng, Y.; Lu, J.; Song, Y.; Xu, W.; Wen, X.; Chen, Z.; Wang, Z. Janus Cellular Design Drives Solar-Powered Spatial Lithium Extraction and Water Co-Generation from Salt-Lake Brines. *Adv. Mater.* **2025**, *2502134*. [CrossRef]
9. Dang, C.; Cao, Y.; Nie, H.; Lang, W.; Zhang, J.; Xu, G.; Zhu, M. Structure Integration and Architecture of Solar-Driven Interfacial Desalination from Miniaturization Designs to Industrial Applications. *Nat. Water* **2024**, *2*, 115–126. [CrossRef]
10. Song, Y.; Fang, S.; Xu, N.; Wang, M.; Chen, S.; Chen, J.; Mi, B.; Zhu, J. Solar Transpiration–Powered Lithium Extraction and Storage. *Science* **2024**, *385*, 1444–1449. [CrossRef]
11. Huang, H.; Li, Z.; Li, Z.; Khan, B.; Huang, K.-W.; Lai, Z.; He, J.-H. Photoelectrochemical Lithium Extraction. *Nano Energy* **2023**, *115*, 108683. [CrossRef]
12. Hu, H.; Guo, X.; Yang, L.; Wu, Y.; Yang, G.; Luo, X. Adsorption Materials toward Highly-Efficient Lithium Extraction from Non-Conventional Lithium Sources. *Adv. Mater.* **2025**, *37*, 2506055. [CrossRef]
13. Xu, X.; Chen, Y.; Wan, P.; Gasem, K.; Wang, K.; He, T.; Adidharma, H.; Fan, M. Extraction of Lithium with Functionalized Lithium Ion-Sieves. *Prog. Mater. Sci.* **2016**, *84*, 276–313. [CrossRef]
14. Shi, Y.; Mai, Z.; Guan, K.; Li, B.; Shen, Q.; Song, Q.; Fu, W.; Xiang, S.; Takagi, R.; Matsuyama, H. Nanomorphogenesis of Interlayered Polyamide Membranes for Precise Ion Sieving in Lithium Extraction. *Water Res.* **2025**, *274*, 123063. [CrossRef]
15. Han, Z.; Qi, S.; Fu, M.; Han, L.; Hong, C.; Shen, Z.; Wang, X.; Su, K.; Xue, X.; Zhang, B.; et al. A Scalable Route to Constructing Hydrogel-Encapsulated Lithium-Ion Sieves-Based Photothermal Fabric Adsorbent for Solar-Enhanced Lithium Extraction from Seawater. *Adv. Funct. Mater.* **2025**, *35*, 2422901. [CrossRef]
16. Bing, S.; Xian, W.; Chen, S.; Song, Y.; Hou, L.; Liu, X.; Ma, S.; Sun, Q.; Zhang, L. Bio-Inspired Construction of Ion Conductive Pathway in Covalent Organic Framework Membranes for Efficient Lithium Extraction. *Matter* **2021**, *4*, 2027–2038. [CrossRef]
17. Bao, S.; Ma, Z.; Yu, L.; Li, Q.; Xia, J.; Song, S.; Sui, K.; Zhao, Y.; Liu, X.; Gao, J. Randomly Oriented Covalent Organic Framework Membrane for Selective Li^+ Sieving from Other Ions. *Nat. Commun.* **2025**, *16*, 3896. [CrossRef]
18. Meng, W.; Chen, S.; Guo, Z.; Gao, F.; Wang, J.; Lu, J.; Hou, Y.; He, Q.; Zhan, X.; Qiu, M.; et al. Three-Dimensional Cationic Covalent Organic Framework Membranes for Rapid and Selective Lithium Extraction from Saline Water. *Nat. Water* **2025**, *3*, 191–200. [CrossRef]
19. Liu, H.; Zhang, K.; Lu, C.; Huang, B.; Liu, J.; Lan, Y.; Lan, W.; Loh, K.P. Electrodialysis Extraction of Lithium from Seawater Using Solid-State Electrolyte-on-Ceramic Membrane with High Aerial Capacity. *ACS Sustain. Chem. Eng.* **2025**, *13*, 9621–9629. [CrossRef]
20. Xu, L.; Wang, M.; Xin, C.; Liu, C.; Wang, W. Mangrove Distribution in Relation to Seasonal Water Salinity and Ion Compartmentation: A Field Study along a Freshwater-Dominated River. *Hydrobiologia* **2020**, *847*, 549–561. [CrossRef]
21. Parida, A.K.; Jha, B. Salt Tolerance Mechanisms in Mangroves: A Review. *Trees* **2010**, *24*, 199–217. [CrossRef]
22. Danilov, D.; Notten, P.H.L. Mathematical Modelling of Ionic Transport in the Electrolyte of Li-Ion Batteries. *Electrochimica Acta* **2008**, *53*, 5569–5578. [CrossRef]
23. Wang, Q.; Wei, D.; Zhao, Z.; Sun, C. Unraveling Concentration Gradient-Driven Ion Transport in Nanopores with Classical Nernst–Planck Equation. *Int. J. Heat Mass Transf.* **2026**, *255*, 127753. [CrossRef]
24. Li, J.-H.; Fan, C.-X.; Huang, L.; Wang, Z.-Y. An Improved Extracellular Ion Fluxes Measurement System Based on Nernst-Planck Equation. *Measurement* **2023**, *216*, 112972. [CrossRef]
25. Vaartstra, G.; Lu, Z.; Grossman, J.C.; Wang, E.N. Numerical Validation of the Dusty-Gas Model for Binary Diffusion in Low Aspect Ratio Capillaries. *Phys. Fluids* **2021**, *33*, 121701. [CrossRef]
26. Chen, T.; Chiu, M.-S.; Weng, C.-N. Derivation of the Generalized Young-Laplace Equation of Curved Interfaces in Nanoscaled Solids. *J. Appl. Phys.* **2006**, *100*, 074308. [CrossRef]
27. Zhao, Y.; Li, W.; Zhan, S.; Jin, Z. Breakthrough Pressure of Oil Displacement by Water through the Ultra-Narrow Kerogen Pore Throat from the Young–Laplace Equation and Molecular Dynamic Simulations. *Phys. Chem. Chem. Phys.* **2022**, *24*, 17195–17209. [CrossRef]
28. Kalugin, D.; Bahig, J.; Shoker, A.; Doan, H.; Kirychuk, S.; Abdelrasoul, A. Superhydrophobic Polyether Sulfone (PES) Dialysis Membrane with Enhanced Hemocompatibility and Reduced Human Serum Protein Interactions: Ex Vivo, in Situ Synchrotron Imaging, Experimental, and Computational Studies. *Sep. Purif. Technol.* **2024**, *335*, 126071. [CrossRef]
29. Huang, Z.; Liu, J.; Liu, Y.; Xu, Y.; Li, R.; Hong, H.; Shen, L.; Lin, H.; Liao, B.-Q. Enhanced Permeability and Antifouling Performance of Polyether Sulfone (PES) Membrane via Elevating Magnetic Ni@MXene Nanoparticles to Upper Layer in Phase Inversion Process. *J. Membr. Sci.* **2021**, *623*, 119080. [CrossRef]

Disclaimer/Publisher's Note: The views, opinions, and information presented in all publications are the sole responsibility of the respective authors and contributors, and do not necessarily reflect the views of UK Scientific Publishing Limited and/or its editors. UK Scientific Publishing Limited and/or its editors hereby disclaim any liability for any harm or damage to individuals or property arising from the implementation of ideas, methods, instructions, or products mentioned in the content.